Accepted manuscript of an article published by Taylor & Francis in Journal of Turbulence (2019), available online: https://doi.org/10.1080/14685248.2019.1706741.

Turbulence structures over realistic and synthetic wall roughness in open channel flow at $\mathbf{Re_\tau = 1000}$

Mostafa Aghaei Jouybari[a]*, Giles J. Brereton[a] and Junlin Yuan[a]

[a]*Department of Mechanical Engineering, Michigan State University, East Lansing, MI 48824, USA*

ARTICLE HISTORY
xx released MM YYYY

ABSTRACT
Turbulence structures in flow over three types of wall roughness: sand-grain, cube roughness and a realistic, multi-scale turbine-blade roughness, are compared to structures observed in flow over a smooth wall in open channel flow at $Re_\tau = 1000$, using direct numerical simulations. Two-point velocity correlations, length scales, inclination angles, and velocity spectra are analyzed. Townsend's outer layer similarity hypothesis [1] is found to apply to: *i*) single-point statistics; *ii*) the general pattern of two-point velocity correlation isocontours, including the average structural inclination; *iii*) velocity spectra; *iv*) helicity; and *v*) the average shape of turbulent eddies. However, it is found that the hypothesis does not apply to two-point correlations of streamwise velocity and length scales of energy-containing motions in the outer boundary layer at the Reynolds numbers of this study. Results from linear stochastic estimation suggest that, near the wall, the quasi-streamwise vortices observed in smooth-wall flow are present in the large-scale recessed regions of multi-scale roughness, whereas they are replaced by a pair of 'head-up, head-down' horseshoe structures in sandgrain and cube roughness, similar to those observed by Talapatra and Katz [2]. The configuration of conditional eddies near the wall suggests that the kinematical process of vortices differ for each kind of rough surface. Eddies over multiscale roughness are conjectured to obey a growth mechanism similar to those over smooth walls, while around the cube roughnessthe head-down horse-shoe vortices of Talapatra and Katz [2] may undergo solid-body rotation on top of a cube roughness on account of the strong shear layer, shortening the longitudinal extent of near-wall structure and promoting turbulence production during this process. Near the wall, the inclination angles, based on contours of two-point velocity correlations, were significantly increased by the presence of roughness, regardless of its texture. For cube roughness, profiles of velocity spectra exhibit dips and peaks at particular wavenumbers on account of the surface periodicity. The multi-scale roughness flow shares some features of a smooth-wall buffer-layer flow inside the roughness sublayer, such as higher energy spectral densities at low wave numbers, an anisotropic vorticity tensor with strong ω_z and prevalence of pairs of counter-rotating inclined streamwise vortices. On the other hand, flows near sand-grain and cube roughness appear to have broken down the streaky motions and their vorticity is more isotropic. These results illustrate the sensitivity of turbulence structure to the roughness texture, particularly within the roughness sublayer.

KEYWORDS
Roughness, wall turbulence, turbulence structure, direct numerical simulation.

*Corresponding author. Email: aghaeijo@egr.msu.edu

1. Introduction

1.1. Literature review

The processes that are essential to sustain turbulence in boundary layers take place close to the wall where the mean shear is high. The turbulent structure responsible for these physical processes [3] have been examined extensively, which has led to improved understanding of turbulence in flows over both smooth and rough surfaces. For smooth walls, this field of study is well established, though it continues to develop in new directions. Some seminal studies in the field include, but are not restricted to, analysis of two point correlations [1], linear stochastic estimation [4], instability analysis [5], mechanisms for generation of coherent packets of hairpins [6], evolutionary behavior of coherent motions [7], and turbulent spot identification [8]. Readers are referred to the monogram by Tardu [9] for a comprehensive review of different methods used to analyze these structures in turbulent flows.

Turbulent structure over rough surfaces has been investigated extensively in previous studies, for a variety of different roughness topographies such as cubical elements [10], turbine blade roughness [11], 2D bars [12], pyramids [2] and 3D sinusoidal surfaces [13]. For a distributed pyramid roughness, Talapatra and Katz [2] found experimental evidence of interacting U-shaped vortices of the scale of the pyramid in the roughness sublayer (RSL). Chan *et. al.* [13] showed that for 3D sinusoidally varying surfaces, the energy contained in larger structures was redistributed to those of the wavelength of the surface, in the vicinity of its crests. Krogstad and Antonia [14] performed experiments on boundary layer flows over k-type rough surfaces: the high sensitivity of values of v'_{rms} and $\overline{u'v'}$ to the wall texture led them to postulate that active motions were strongly dependent on the geometry of the rough wall.

Many rough surfaces found in nature are multiscale or fractal-like [15]. Several recent studies on how multiscale roughness textures affect turbulence have focused on the frictional drag and turbulence statistics within the roughness sublayer. It has been found that the drag scales predominantly on wall-normal turbulence fluctuations at the elevation of the roughness crest [16, 17], and that surface roughness at longer wavelengths does not play a significant role in drag production [18]. For turbine-blade surfaces [19], filtered graphite surfaces [20], and other dissimilar random surface roughnesses [17], it has been shown that the anisotropies of the Reynolds and dispersive stress tensors are texture-dependent. In general, Townsend's similarity hypothesis has been observed to apply to these statistics, provided that the ratio of boundary-layer to sublayer thickness was large and that the Reynolds number is sufficiently high.

For many rough surfaces, only statistical inferences of effects of roughness on the flow have been made, and those studies on turbulence structure focused mostly on particular types of roughness topography, with few studies on multiscale roughness. Relatively little is understood about turbulent structure and coherent motions over different types of rough surfaces, and how their modification by synthetic and realistic wall roughnesses might differ.

1.2. Objectives

The present study is intended to provide a more comprehensive understanding of turbulence structures in fully-developed channel flows over rough walls. The main objectives are first to explore how roughness modifies turbulent coherent motions in flows over rough walls, and second to compare the behavior of these motions in flow

over a realistic rough surface and in flow over a 'standard' roughness. The realistic surface is characterized by multiple scales/wavelengths of roughness while a standard roughness, made up of distributed elements of similar shapes, is described by a single or narrow set of dominant wavelengths. To this end, turbulent flow over a flat surface with the roughness of a production hydraulic turbine blade is simulated and compared with flow over a smooth wall and over two other quite different rough surfaces: sand-grain and cube roughness. Flows in both the roughness sublayer and the outer layer are examined and two-point velocity correlations, length scales, inclination angles, velocity spectra, vorticities, and helicities are analysed. Linear stochastic estimation is employed to explore the average behavior of instantaneous vortical motions in those regions and their dependence on roughness topography.

An understanding of how roughness modifies turbulence structures can also provide important insights into modeling and control of turbulence in both equilibrium and non-equilibrium (accelerating/decelerating) flows over rough walls, though it is recognized that, in non-equilibrium turbulent flows, some effects of roughness can propagate throughout the entire boundary layer, in which case equilibrium wall-similarity scalings may not apply.

2. Methodology

2.1. Governing equations

Direct numerical simulation is used to solve the incompressible, constant-property continuity and Navier-Stokes equations for a Newtonian fluid. The equations in indicial notation are

$$\frac{\partial u_i}{\partial x_i} = 0, \tag{1a}$$

$$\frac{\partial u_i}{\partial t} + \frac{\partial u_i u_j}{\partial x_j} = -\frac{\partial P}{\partial x_i} + \nu \frac{\partial u_i}{\partial x_j \partial x_j} + F_i, \qquad (i,j = 1,2,3) \tag{1b}$$

where x_1, x_2 and x_3 (or x, y, z) are the streamwise, wall-normal and spanwise directions respectively, the corresponding velocity components are u_1, u_2 and u_3 (or u, v, w), $P = p/\rho$ is the modified pressure, ρ is the fluid density and ν is the kinematic viscosity. The body force F_i is added to the right-hand side of the momentum equations to impose boundary conditions at a rough surface using the immersed boundary method [21]. Details of the implementation and validation of this method are provided in Yuan and Piomelli [22, 23]. A second-order central-difference scheme was used for spatial discretizations, and a second-order Adams-Bashforth semi-implicit time advancement was employed to solve equation (1) on staggered grids. The numerical solver used MPI parallelization and has been validated for turbulent flow simulations [24].

A double-averaging decomposition [25] was used to calculate statistical quantities within the roughness sublayer, where the flow is spatially heterogeneous. In this representation, the instantaneous value of a flow variable θ is decomposed into three components,

$$\theta(\boldsymbol{x}, t) = \langle \overline{\theta} \rangle(y) + \theta'(\boldsymbol{x}, t) + \widetilde{\theta}(\boldsymbol{x}). \tag{2}$$

Here $\overline{\theta}$ is the time- or Reynolds-averaging operator, and $\langle \theta \rangle = \frac{1}{A_f} \int_{A_f} \theta dA$, where A_f

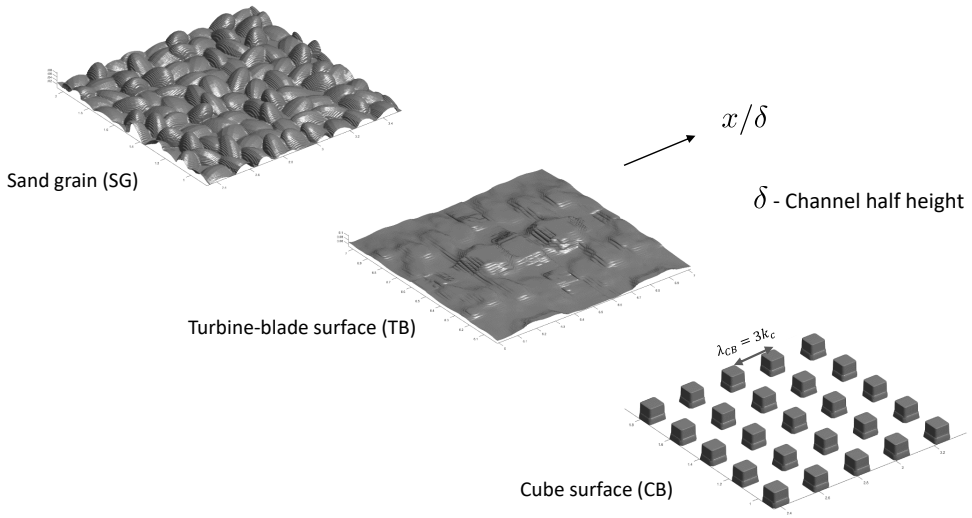

Figure 1. Simulated rough surfaces. The figures show a portion of $\delta \times \delta$ in the x-z plane.

Table 1. Geometric parameters of rough surfaces. $\mathrm{Ra} = \langle |k - \langle k \rangle| \rangle$ is the first-order moment of height fluctuations; k_{rms}, root-mean-square of height; s_k, skewness; k_u, kurtosis; ES_{x_i}, effective slope in the x_i direction.

Surface	k_c/δ	Ra/δ	k_{rms}/Ra	s_k	k_u	ES_x	ES_z
SG	0.09	0.014	1.05	0.48	2.97	0.43	0.44
TB	0.12	0.014	1.17	0.20	3.49	0.10	0.08
CB	0.07	0.014	0.36	2.45	7.01	-	-

is the area occupied by fluid, and so is the *intrinsic* spatial averaging operator in the homogeneous x and z directions. The Reynolds fluctuating component is $\theta' = \theta - \overline{\theta}$ and the dispersive fluctuating component is $\widetilde{\theta} = \overline{\theta} - \langle \overline{\theta} \rangle$.

2.2. Surface roughness

The three types of wall roughness considered in this study are shown in Figure 1. For all rough cases, the y origin is set at the lowest trough of the surface. The sand-grain roughness (SG) [21] comprises densely packed, randomly oriented ellipsoidal elements of the same shape, with semi-axis lengths of $(\lambda_1, \lambda_2, \lambda_3) = (1.0, 0.7, 0.5)k_c$, where k_c is the roughness crest height. The turbine blade roughness (TB) is the surface S4 of Yuan and Piomelli [19], mirrored once with respect to both the x and z directions to accommodate periodic boundary conditions. It features surface lengthscales in x and z which exceed the channel half-height δ. The cube roughness (CB) was generated by homogeneous duplication of a cube element in the x and z directions with steps of $\lambda_{CB} = 3k_c$ to yield a k-type roughness [26]. Characteristic geometric parameters of these three rough surfaces are displayed in Table 1. Each surface has the same first-order moment of height fluctuation $\mathrm{Ra} = 0.014\delta$, a crest height of roughly 0.1δ, and a positively skewed height distribution ($s_k > 0$). The effective surface slope ES_{x_i} [27] is

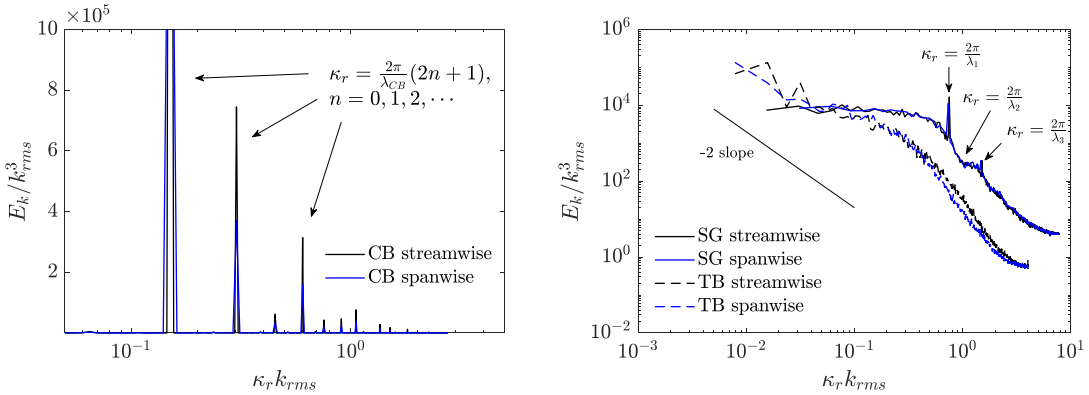

Figure 2. Surface height power spectra for CB (*left*), SG and TB (*right*) roughnesses.

Table 2. Simulation parameters.

	Re_τ	Re_b	k_s^+	y_R/δ	d/δ	$(L_x, L_z)/\delta$	(n_i, n_j, n_k)	$(\Delta x^+, \Delta y^+_{min}, \Delta z^+)$	$C_d \times 10^3$
SM	1000	20000				$(6, 3)$	$(512, 256, 512)$	$(11.7, 0.3, 5.8)$	2.5
SG	1000	11200	78	0.12	0.044	$(6, 3)$	$(1024, 236, 512)$	$(6.0, 0.7, 6.0)$	8.0
TB	1000	14400	24	0.14	0.058	$(13, 13)$	$(1024, 259, 1024)$	$(13.0, 0.8, 13.0)$	4.8
CB	1000	10900	96	0.10	0.039	$(6, 3)$	$(1024, 373, 512)$	$(6.0, 0.8, 6.0)$	8.4

Superscript + indicates normalization in wall units, $\delta_\nu = \nu/u_\tau$, friction velocity $u_\tau = \sqrt{\tau_w/\rho}$, $L_y = \delta$, zero-plane displacement height is d, drag coefficient $C_d = (u_\tau/U_b)^2$, $\mathrm{Re}_\tau = u_\tau\delta/\nu$, $\mathrm{Re}_b = U_b\delta/\nu$ and bulk velocity is U_b.

defined as

$$\mathrm{ES}_{x_i} = \frac{1}{L_x L_z}\int_{L_x,L_z}\left|\frac{\partial k(x,z)}{\partial x_i}\right| dzdx, \tag{3}$$

where $k(x, z)$ is the local height of the surface, and differs appreciably for these three surfaces. The value of ES_{x_i} for TB roughness is half that for SG roughness. The ES values for the CB roughness is not compared due to its value being locally infinity.

The probability density functions (PDFs) of the local surface gradients $\partial k/\partial x_i$, for SG and TB roughness, are given in Yuan and Aghaei Jouybari [28], where it is shown that gradients steeper than 14° in inclination to the horizontal plane occur more frequently in SG roughness than in TB roughness. The CB roughness has the steepest local surface gradients. Streamwise and spanwise power spectra of these surface height variations are shown in Figure 2. They feature spikes at $\kappa_r = 2\pi/\lambda_{CB}$ for CB roughness, distinct peaks at $\kappa_r = 2\pi/\lambda_1$ for SG roughness, and an extended region with a slope of roughly -2 for TB roughness. We therefore characterize both the CB and SG surfaces as spiky surfaces (in terms of its spectral shape, other than physical shape) and the TB surface as fractal [29] surfaces, respectively.

2.3. Simulation parameters

The parameters used in these simulations are shown in Table 2. All simulations were carried out at $\mathrm{Re}_\tau = 1000$ using n_i, n_j and n_k grid points in streamwise (x), wall-normal (y) and spanwise (z) directions, with corresponding domain sizes of L_x, L_y and L_z. The choice of the same value of Re_τ for all simulations provided a good

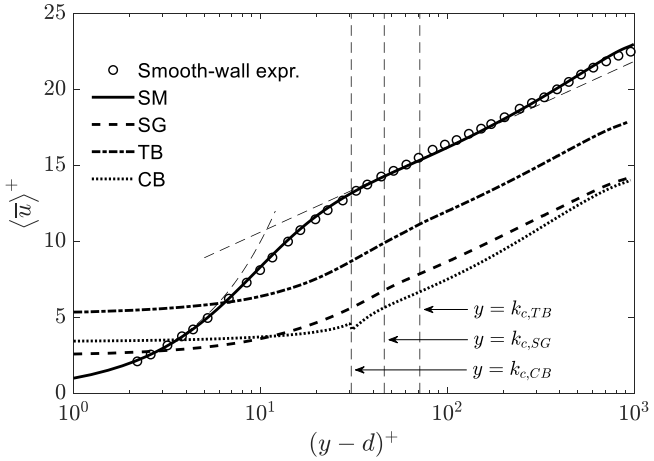

Figure 3. Mean streamwise velocity profiles in wall units. Smooth-wall experimental data are from Schultz and Flack [33].

basis for comparison between rough- and smooth-wall flows at a moderate Reynolds number. According to their respective roughness Reynolds number, k_s^+ (to be quantified later), all rough cases are in the fully-rough regime according to the findings of Yuan and Piomelli [19] for SG and TB roughness, and the k-type roughness studies of Bandyopadhyay [30, fully rough when $k_s^+ > 50$] for CB roughness. This indicates that the near-wall mean-flow patterns are fully developed, not modified by a further increase of k_s^+. As such, the difference in turbulent structure identified in this study is considered predominantly a result of the difference in roughness geometry, other than the difference in k_s^+. The grid points were distributed uniformly in the streamwise and spanwise directions. In the wall-normal direction, they were spaced uniformly for $y < k_c$ but stretched for $y > k_c$ with larger grid sizes farther from the wall. For all simulations, the grid sizes $(\Delta x, \Delta y, \Delta z)/\eta$, where η is the Kolmogorov length scale (see Figure 8b), were less than 11 in the x and z directions and much smaller in the wall-normal direction. Based on the observation of Moser and Moin [31], scales smaller than 15η contributed predominantly to turbulent dissipation. Therefore the grid resolutions used in the current study are small enough to resolve the dissipative scales. In these half-channel simulations, periodic boundary conditions were imposed in the x and z directions, and symmetry and no-slip boundary conditions were applied at the top and bottom boundaries respectively. After the initial transient of the simulation was completed, data were collected for statistical analysis over a simulation time of 10-50 large-eddy turnover times ($T \approx \delta/u_\tau$).

2.4. Statistics of mean velocity of turbulence

The roughness sublayer height y_R is defined as the entire near-wall layer with non-negligible form-induced velocities. y_R is quantified as the location where $\langle \widetilde{u}^2 \rangle^{0.5}$ first meets $0.06\langle \overline{u} \rangle$, similar to the method proposed by Pokrajac et al. [32]. $y_R \leq 0.15\delta$ for all present simulations.

Mean streamwise velocity profiles, normalized in wall units, are shown in Figure 3. Each profile has a distinct logarithmic region over the range $30 < (y-d)^+ < 200$, indicating conformity with the law of the wall. It follows that an equivalent sand-grain

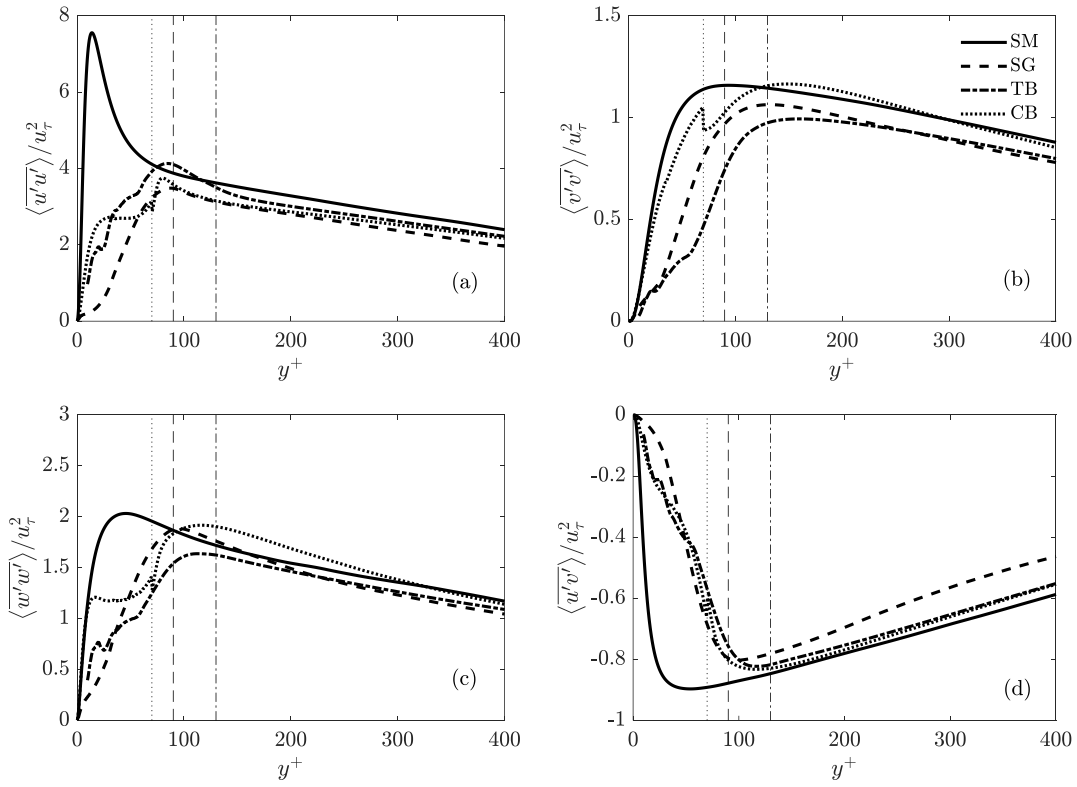

Figure 4. Profiles of normal (a,b,d) and shear (d) Reynolds stress tensor components in wall units.

height k_s can be inferred from the data of Figure 3 and Nikuradse's correlation (Eq. 4) [34] in the logarithmic region:

$$\langle \overline{u} \rangle^+ = \frac{1}{\kappa} \ln \left(\frac{y-d}{k_s} \right) + 8.5, \tag{4}$$

where d is the displacement height defined as the location where the mean drag appears [35], and $\kappa = 0.41$ is the von Karman constant. In Table 2, the inferred values of k_s^+ are given as 24, 78 and 96 for TB, SG and CB roughness respectively, rendering all rough cases fully rough. The comparison of the drag coefficient C_d given in Table 2 appears to follow that of k_s^+, with $C_{d,TB} < C_{d,SG} < C_{d,CB}$. This trend may be explained as a result of the very different effective slope values [27], $ES_{TB} < ES_{SG} < ES_{CB}$. It will be shown in the following sections that the effects of roughness on various turbulence structural parameters also follow such relation, with flow characteristics in the TB case generally intermediate between those in the smooth and SG cases, while the effect of CB roughness tend to be more significant than SG and TB roughnesses.

Figure 4 shows profiles of the normal and shear components of the Reynolds stress tensor in wall units. Overall, the outer layer similarity is satisfied. In the roughness sublayer, the roughness expectedly changes the Reynolds stresses, resulting in a lower anisotropy for rough walls compared to the smooth one. Consequently, the effect of surface topography is greater on the streamwise normal stress than on the other three.

The slight outer-layer mismatch between smooth-wall values of $\langle \overline{u'v'} \rangle^+$ and the val-

ues on the rough walls as shown in Figure 4 (d) is due to non-zero dispersive shear stress, $\langle \widetilde{u}\,\widetilde{v} \rangle^+$ in the outer layer. These non-zero values of $\widetilde{u}$ and $\widetilde{v}$ result from very-large-scale motions with low or high momentum, elongated in the streamwise directions. These motions are thought to originate from the spanwise heterogeneity of rough surfaces with spanwise wavelengths λ_z which are comparable to δ, same as the surface-induced mean secondary flows first observed for turbine-blade roughness [36, 37] and later systematically studied by Vanderwel and Ganapathisubramani [38] and Yang and Anderson [39], among others, on organized distributed roughness. Consistent with these studies, for the present SG and TB surfaces it is found that the spanwise locations of high surface drag (averaged in x) coincide with the locations of the high-momentum pathways (not shown), even for the SG roughness which is not characterized by a predominant spanwise wavelength of $o(\delta)$. The spanwise separation between alternating low and high momentum regions are at least 1δ, consistent with what is expected of the surface-induced secondary motions. However, the present simulation setup using streamwise periodic channels inevitably leads to 'spanwise locking' [40] of coherent motions with lengths longer than the streamwise domain size (6δ, much shorter than the very-large-scale motions). Consequently, these observed pathways are influenced, if not significantly modified, by the simulation setup and thus not discussed in depth herein.

3. Results

In the following, the characteristics of turbulence structure are discussed using two-point velocity correlation, various length scales, energy spectra, vorticity, and both instantaneous and conditionally-averaged vortical motions.

3.1. Two-point velocity correlations

The general form of a two-point correlation of turbulent velocities is defined as

$$R_{u_\alpha u_\beta}(y, r_1, r_2, r_3) \equiv \left\langle \overline{u'_\alpha(x, y, z, t) u'_\beta(x + r_1, y + r_2, z + r_3, t)} \right\rangle. \tag{5}$$

The normalized two-point correlations (denoted by subscript n) with a separation in x is

$$R_{u_\alpha u_\beta, n}(y, r_1) = R_{u_\alpha u_\beta}(y, r_1, 0, 0) / R_{u_\alpha u_\beta}(y, 0, 0, 0) \ . \tag{6}$$

In Figure 5, the profile of $R_{uu,n}(y, r_1)$ is shown at different distances from the wall. It can be seen that, close to the wall, $R_{uu,n}$ is most affected by local features of roughness, depicted by the black lines. In an unperturbed turbulent flow field, the magnitude of $R_{u_\alpha u_\beta, n}$ decays smoothly from unity at zero separation, as shown in Figure 5 for flow over a smooth wall. However, the effect of surface roughness can be to either enhance or reduce the value of the correlation at different displacements, due to the periodicity and length scales of roughness.

Near a rough wall, the two-point velocity correlation at a given displacement $\boldsymbol{r}$ can be attributed to: *i*) coherent motions of turbulence of scale $\boldsymbol{r}$; and *ii*) periodic excitation from the surface roughness at wavelength $\boldsymbol{r}$. For example, in the case of CB roughness shown in Figure 5, near the wall the correlation at displacements shorter

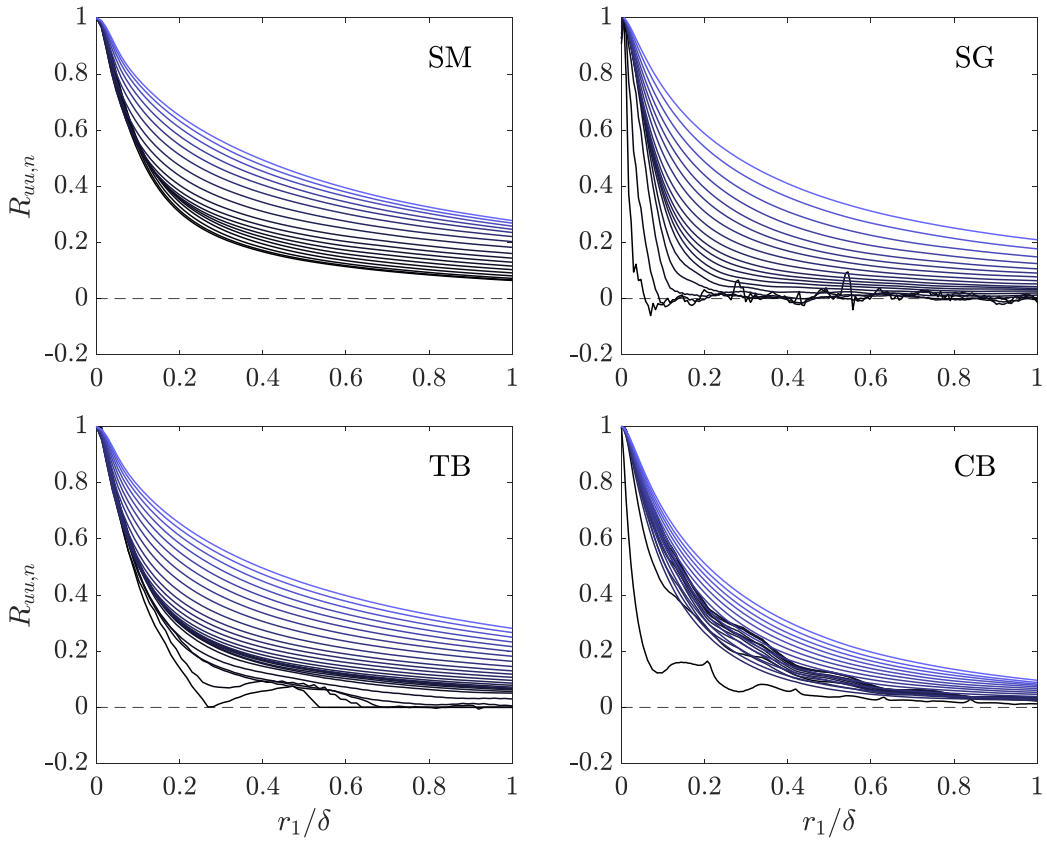

Figure 5. Profiles of $R_{uu,n}(y, r_1)$ at y locations from $y \approx 0$ (*black*) to $y/\delta = 0.3$ (*blue*).

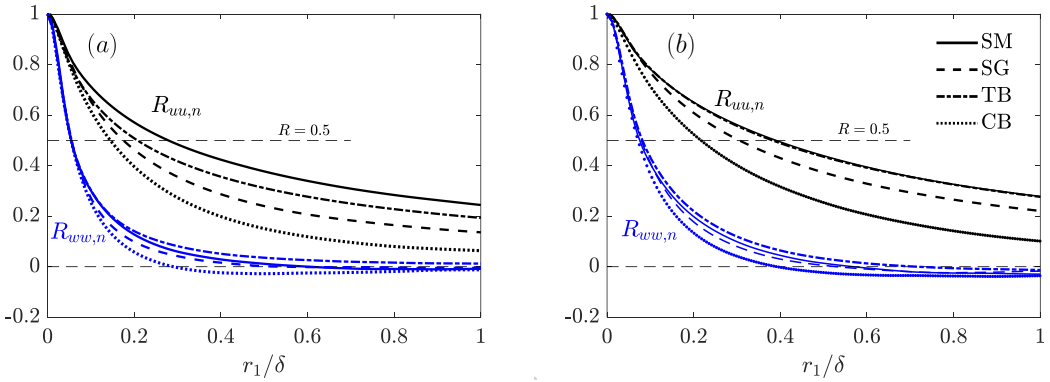

Figure 6. Profiles of $R_{uu,n}(r_1)$ (*black*) and $R_{ww,n}(r_1)$ (*blue*), at $y/\delta = 0.15$ (a), at $y/\delta = 0.3$ (b).

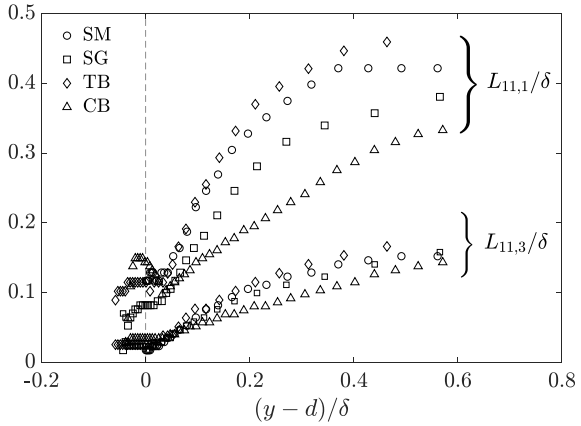

Figure 7. Averaged streamwise ($L_{11,1}$) and spanwise ($L_{11,3}$) energy-containing length scales.

than 0.1δ associates predominantly to local streaky motions, while for r_1 of approximately $\lambda_{CB} = 0.21\delta$, the periodic spatial distribution of these streaky motions (smaller than 0.21δ) on account of periodic cube arrangements contribute to the correlation. Pronounced local peaks of R_{vv} with a separation of the wavelength of distributed roughness such as 2D bars was also observed [41]. It will be shown in section 3.3 that this effect results in peaks and troughs in velocity spectra measured within the roughness sublayer.

Streamwise and spanwise velocity correlations are plotted in Figure 6 for two outer-layer locations, $y/\delta = 0.15$ and $y/\delta = 0.3$. In Figure 6(a), it is shown that $R_{uu,n}$ is still affected by surface roughness at $y/\delta = 0.15$ and in Figure 6(b), it is shown that $R_{uu,n}$ in flow over the smooth wall and TB roughness collapse at $y/\delta = 0.3$, whereas in flows over walls with SG and CB surfaces they do not—they exhibit a lower degree of correlation over the entire channel. The spanwise velocity correlations $R_{ww,n}$ yield a better overall collapse for the different surfaces than streamwise correlations at both locations. According to the Townsend's outer-layer similarity hypothesis [1], velocity correlations at this location would be expected to collapse when δ/k (where k is the roughness height) is sufficiently large. Jiménez [42] has proposed that Townsend's similarity hypothesis applies when $\delta/k \geq 50$. In the present study, the maximum value of δ/k_c is 14 (for CB roughness), which may explain departures from the hypothesis for the two-point correlation, although it has been shown that wall similarity applies to single-point statistics such as components of the Reynolds stress tensor. It follows that outer-layer structural characteristics of turbulence (such as two-point velocity correlations) appears to be more sensitive to roughness influence than single-point statistics.

3.2. Length scales and inclination angles

The size of large-scale energy-containing coherent motions are previously quantified in various ways: (1) a length scale defined by a cutoff value of $R_{u_iu_j,n}$ [43, 44, 12], (2) integral length scales of $R_{u_iu_j,n}$ [45, 22], (3) the length scales of low-momentum regions of a linear-stochastically-estimated velocity field [46], (4) the length scales obtained from the spectral coefficients of the correlations [47, 48]. In the present study, two types

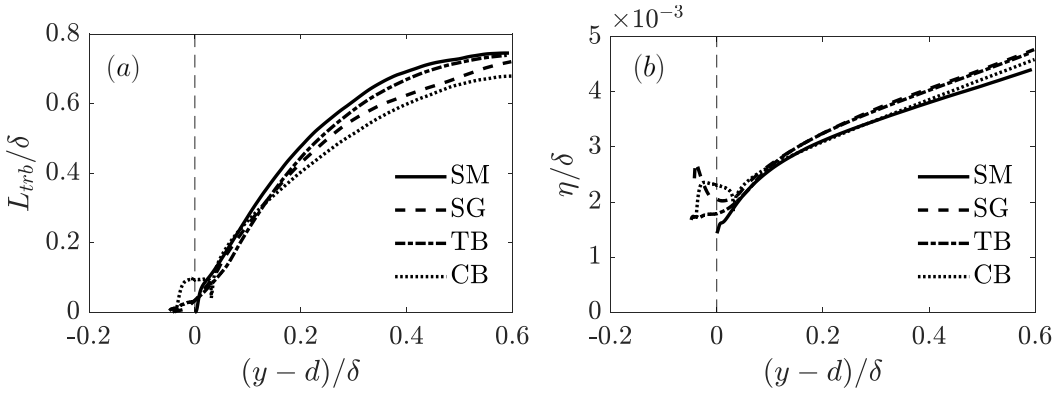

Figure 8. Turbulent (a) and Kolmogorov (b) length scales.

of length scales are analyzed: (1) the x- and z-extent of the isocontour of $R_{u_iu_j,n} = 0.5$ [44, 12], $L_{ij,k}$ with separation in x_k, as a two-point structural property, and (2) the turbulent length scale, $L_{trb} \equiv k^{3/2}/\epsilon$, as a single-point statistical property, where k is the turbulence kinetic energy (TKE) and ϵ is the TKE dissipation rate. The choice of $R_{u_iu_j,n}$ cutoff value in $L_{ij,k}$ does not change the overall comparison of $L_{11,1}$, as shown by the shape of $R_{u_iu_j,n}$ profiles in Figure 6.

These two length scales are plotted in Figures 7 and 8(a), respectively. In both figures, the length scales show linear behavior near the wall ($y^+ < 150$ or $y/\delta < 0.15$), which implies the self-similar growth of the large-scale motions in an average sense. The linear increase of spanwise length scales were also observed by Tomkins and Adrian [46]. Also, it is shown here that L_{11} is smaller above CB and SG surfaces than those above the smooth wall and TB surface. It should be noted that, although L_{trb} (as a direction-free length scale) and $L_{11,3}$ (as a spanwise length scale) appear to conform with the Townsend's outer-layer similarity hypothesis, $L_{11,1}$ and $R_{uu,n}$ (Figure 6) do not. This suggests that the response of the outer layer flow to wall roughness is directionally sensitive and that the streamwise structure can be influenced strongly by the roughness texture. The experimental study of Krogstad and Antonia [43] on boundary layer flows over smooth and rough walls with $\delta/k \approx 50$ also showed that $L_{11,1}$ (based on a cutoff value of $R_{uu,n} = 0.3$) for rough walls was smaller than for smooth walls in outer layer, and $L_{11,3}$ was almost the same in both cases. The departure from Townsend's similarity in both our results and Krogstad and Antonia [43] may be due to limited Reynolds number, as repeated experiment of turbulent boundary layer flow over a square bar roughness by Krogstad and Efros [49] at a high Reynolds number ($Re_\theta = 32600$ and $\delta/k = 131$) indicated reduced roughness influence on the outer layer.

To compare the size of energy-containing motions mentioned above with the size of the dissipative-scale motions, the Kolmogorov length scale $\eta = (\nu^3/\epsilon)^{1/4}$ is plotted in Figure 8(b). It can be seen that profiles of η are sensitive to the surface textures only below the roughness crest. Note that, in this region, turbulence departs significantly from a homogeneous isotropic state due to the mean-flow heterogeneity; consequently, η may no longer represent the dissipative scales. For $y > k_c$, all η profiles collapse, indicating that small scale structures become independent of the surface texture even though large-scale structures do not. This observation agrees with the first hypothesis of Kolmogorov [50] that, at scales of the order of η, turbulence obeys a universal

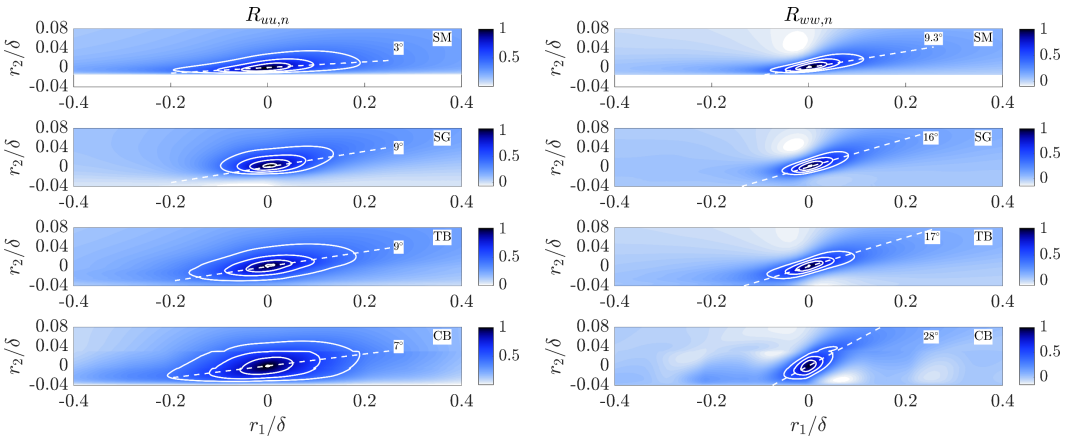

Figure 9. Contours of $R_{uu,n}(r_1, r_2)$ (*left*) and $R_{ww,n}(r_1, r_2)$ (*right*) centered at $y = d$ for SG, TB and CB roughness, and at $y^+ = 15$ for the smooth case. The contour level range is [0.4 1.0] with a step size of 0.2.

equilibrium and is locally isotropic.

To quantify the inclination angles of large-scale coherent motions, contours of $R_{uu,n}(y, r_1, r_2)$ and $R_{ww,n}(y, r_1, r_2)$ were plotted in the x-y plane, centered at two types of elevations: (1) a near-wall location in the roughness sublayer ($y = d$) for rough cases and in the buffer layer ($y^+ = 15$) for the smooth case, shown in Figures 9, and (2) an outer-layer location, at $y/\delta = 0.3$ for all cases, shown in Figure 10. The characteristic inclination angles were obtained by plotting the best-fitted line (using linear least square method), traversing the farthest points from the origin at contour levels of {0.2, 0.4, 0.6, 0.8}. These angles are examined in the context of: *i*) how the angle depends on the particular correlation, for a given surface; and *ii*) how the inclination angle depends on the surface texture.

The figures show that the inclination angles of $R_{uu,n}$ are much smaller than those of $R_{ww,n}$ at both the near-wall and outer-layer elevations. A physical explanation is that w' fluctuations originate from ω_x and ω_y motions, associated with individual vortical motions such as quasi-streamwise vortices, while the u' motions are associated with streaky motions. As a result, the x-extent of u' and w' motions are very different and characterized by different inclination angles.

For the near-wall elevations, the angles of inclination depends significantly on the presence of roughness and its texture. These angles are approximately 3° for $R_{uu,n}$ and 9° for $R_{ww,n}$ near the smooth wall and much higher on rough walls, equaling $7° - 9°$ and $16° - 28°$, for $R_{uu,n}$ and $R_{ww,n}$ respectively (Figure 9). Here, the CB roughness yields much higher $R_{ww,n}$ inclination angle of 28° than the other rough surfaces. Near the wall, Yuan and Piomelli [22] also observed higher inclination angles in the roughness sublayer than in the viscous sublayer, for the SG roughness in sink-flow boundary layers. In the outer layer, all cases show similar inclinations of 8° – 11° for $R_{uu,n}$ and 26° - 31° for $R_{ww,n}$ (Figure 10). The outer-layer values are consistent with those reported by Volino *et. al.* [12], where angles of turbulent structures for boundary layer flows over 3D cubes and 2D bars were also deduced from $R_{uu,n}$ contours. They found

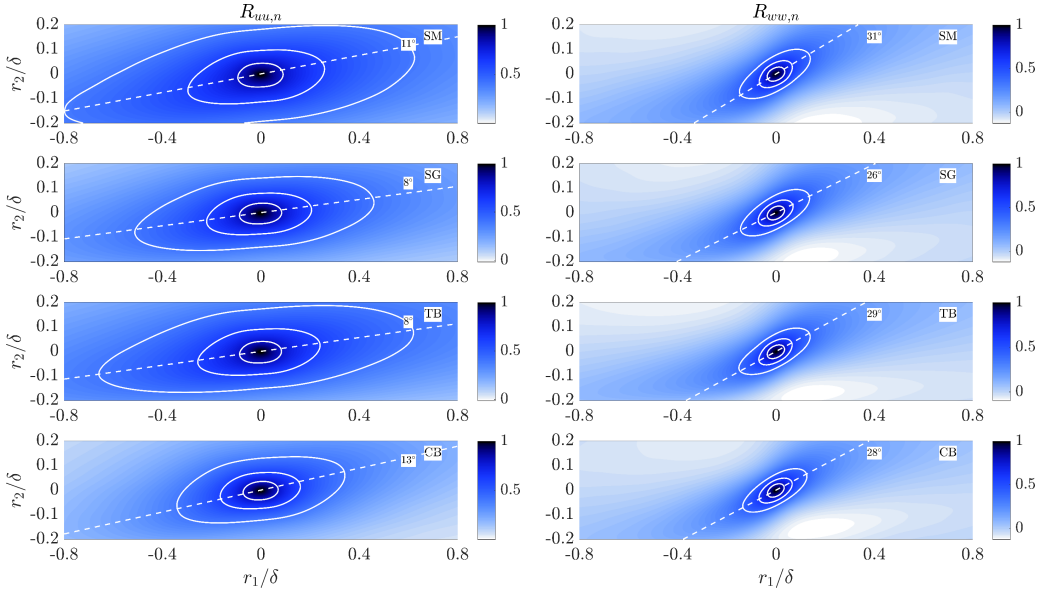

Figure 10. Contours of $R_{uu,n}(r_1, r_2)$ (*left*) and $R_{ww,n}(r_1, r_2)$ (*right*) centered at $y/\delta = 0.3$. The contour level range is [0.4 1.0] with a step size of 0.2.

that for $0.2 < y/\delta < 0.5$ the inclination angle of $R_{uu,n}$ contour was surface-texture independent and ranged between 10 to 14 degrees. Similar observations were made by Coceal *et. al.* [10] for channel flow over cubes. These values are largely comparable to the angles found here for very different roughness geometries.

3.3. Velocity spectra

One-dimensional velocity spectra are defined as twice the Fourier transform of $R_{u_i u_j}(y, r_1)$, as

$$E_{ij}(y, \kappa_1) \equiv \frac{1}{\pi} \int_{-\infty}^{\infty} R_{u_i u_j}(y, r_1) e^{-i\kappa_1 r_1} dr_1. \tag{7}$$

Using equation (7) to calculate E_{ij} is computationally more expensive than the equivalent expression from cross-correlation theory (the Wiener-Khinchin theorem when $i = j$):

$$E_{ij} = 2\mathscr{F}(R_{u_i u_j}) = 2\mathscr{F}^*(u_i') \cdot \mathscr{F}(u_j'), \tag{8}$$

where $\mathscr{F}$ is the Fourier transform operator and * indicates the complex conjugate. The right hand side of equation (8) is cheaper to compute as it can be obtained by a Fast Fourier Transform (FFT) algorithm. Equation (8) was also used to obtain R_{ij} by taking the inverse Fourier transform of its right-hand side [51]. We verified the numerical equivalence of equations (7) and (8) for $y > k_c$ (where the velocity fields are simply connected) by calculating the energy spectra using both methods, which yield very similar results. Below the roughness crest, however, the interpretation of E_{ij} obtained from equation (8) is less clear because fluid domains in the $x - z$ plane is multiply connected. On the other hand, equation (7) is appropriate because $R_{u_i u_j}$ is

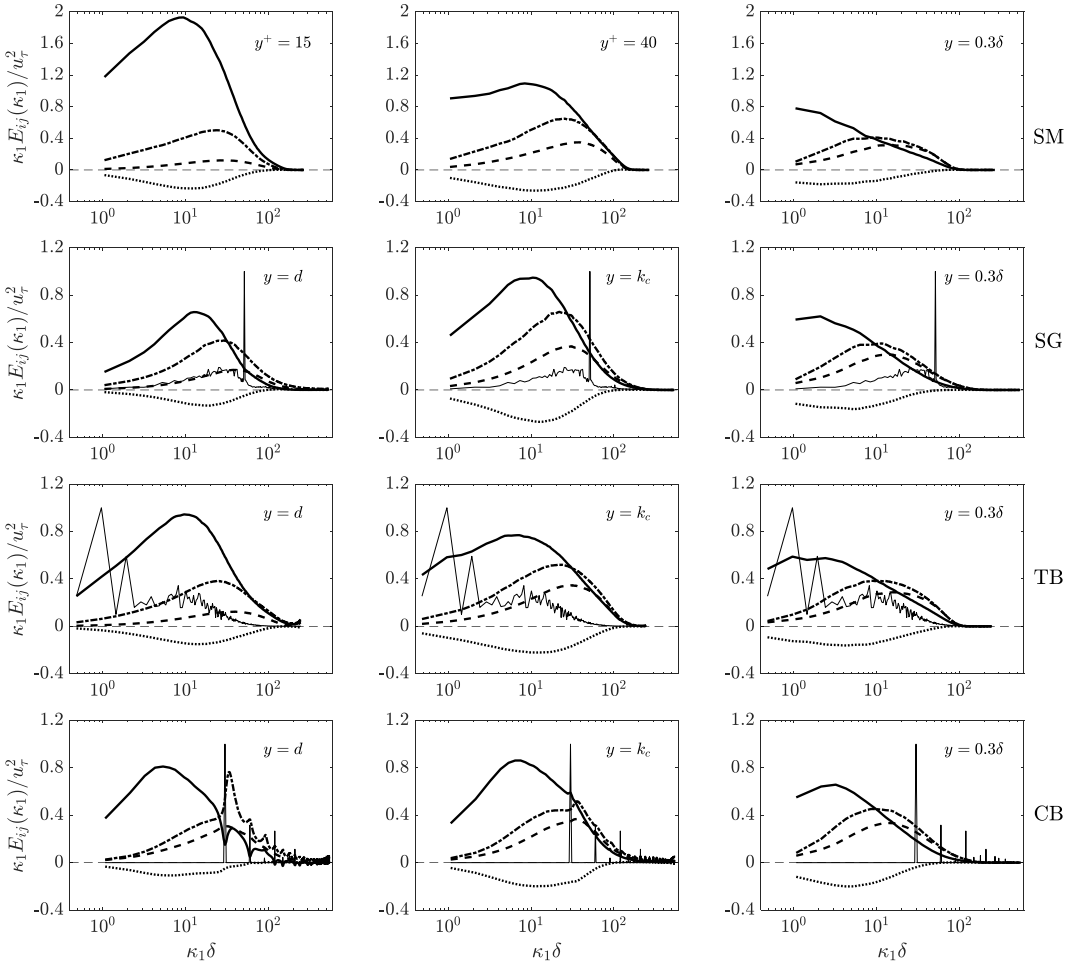

Figure 11. One-dimensional longitudinal premultiplied velocity spectra, E_{ij}, and surface-height power spectra, E_s. ——— E_{11}; - - - E_{22}; -·- E_{33}; ··· E_{12}; ——— (thin) E_s. E_s is normalized to give a maximum value of 1.

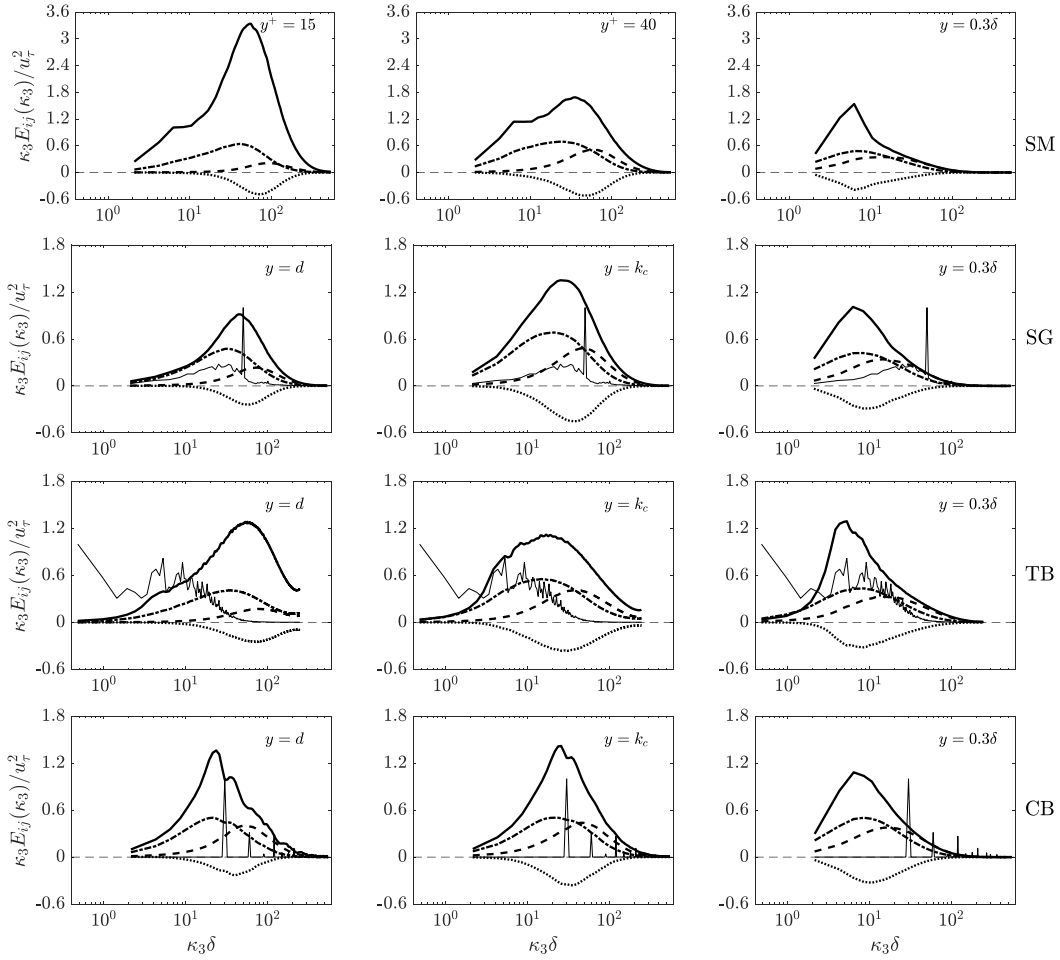

Figure 12. One-dimensional transverse premultiplied velocity spectra. ——— E_{11}; - - - E_{22}; - - - E_{33}; - - - E_{12}; ——— (thin) E_s. E_s is normalized to give a maximum value of 1.

continuous regardless of the elevation. To our knowledge, no velocity spectra appear to have been reported to date in the region where $y < k_c$. Here, we use equation (7) for spectral estimation in regions both below and above k_c. In this study, the velocity spectra at all y-locations are obtained using a Hann window function to minimize the Gibbs phenomenon at large wavenumbers [52]. Data within half of the x and z domains are used to calculate the two-point correlations; thus, noises are present in the spectra if no window function is used.

The premultiplied velocity spectra E_{11}, E_{22}, E_{33}, and E_{12} are plotted in Figures 11 and 12 in the κ_1 and κ_3 directions, respectively. They are compared with the power spectra of surface height fluctuations to explore a possible relation between the length scales of turbulence and those of the rough surface. Three types of elevations are of particular interest. First, at $y = d$, the rough-case results are compared with those in the smooth case inside the buffer layer at $y^+ = 15$. Secondly, the lower edge of the logarithmic region (around $y = k_c$, see Figure 3) in the rough cases is compared with $y^+ = 40$ in the smooth case, which is also at the lower edge of the logarithmic region. And thirdly, the outer layer at $y/\delta = 0.3$ is compared among all cases, where the flow is expected to be independent of surface conditions if Townsend's similarity hypothesis

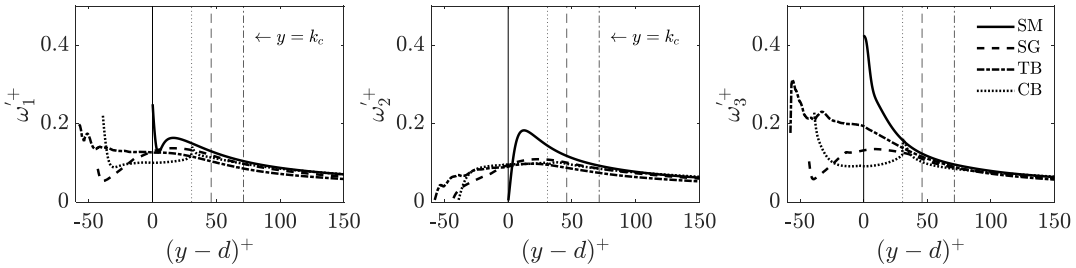

Figure 13. Profiles of RMS vorticity in wall units. Thin vertical lines show the corresponding roughness crest elevations.

applies.

In Figures 11 and 12, it can be seen that at the near-wall locations, the peak values of E_{ij} components, normalized by u_τ and κ, show higher anisotropy in SM and TB cases, consistent the Reynolds stress comparison in Figure 4. At $y = d$ and $y = k_c$ the E_{ij} components are dependent on the kind of surface chosen and, as y increases, they become progressively more independent of the surface condition. For example, at $y/\delta = 0.3$, the location of the energy peaks and the general shapes of E_{ij} are similar for each kind of wall roughness, consistent with Townsend's similarity hypothesis. As y decreases, the peak of E_{11} moves toward higher wavenumbers in both the κ_1 and κ_3 directions, indicating shrinking of energy-containing scales as the wall is approached. The energy carried by the low-wavenumber u' motions is, in all rough cases at both $y = d$ and $y = k_c$, much less than in the smooth-wall case at the corresponding elevations, because surface roughness breaks down the buffer-layer streaky motions by introducing voritcal structures with high three-dimensionality.

At the near-wall elevation, the connection between the energy spectra and the surface length scales is analyzed for each kind of roughness. For SG roughness, it appears that the peaks of $E_{22}(\kappa_1)$ and $E_s(\kappa_1)$ coincide at the same wavenumber. Similarly, the peak of the $E_{11}(\kappa_3)$ coincides with both that of $E_s(\kappa_3)$, though such wavelength is also where the smooth-wall $E_{11}(\kappa_3)$ peak is located. For TB roughness, the fractal nature of the surface-height distribution does not yield a dominant surface wavenumber; its E_{ij} profiles are similar to those in the smooth case. For CB roughness, the energy spectra are strongly correlated with the surface power spectrum, which has spikes at $\kappa = 2\pi/\lambda_{CB}$ and its multiples. At $y = d$, in Figure 11 it can be seen that E_{11} and E_{33} have toughs and peaks, respectively, at the same κ_1 values as these spikes. These extrema appear to be a consequence of the surface periodicity described in section 3.1.

3.4. Vorticity and helicity

The root-mean-square (RMS) values of vorticity fluctuations, normalized in wall units, are plotted in Figure 13. In the outer layer, irrespective of the surface type, all cases collapse showing the isotropy of the vorticity tensor—a result observed previously for both smooth [53] and rough walls [54]. It is known that, near a smooth wall ω_3' is mostly caused by the intense shear generated by u' between the wall and the streaks, ω_2' represents mostly $\partial u'/\partial z$ in the regions between adjacent high and low-speed streaks, and ω_1' displays a local minimum and a local maximum at $y^+ = 5$ and 20 respectively, attributed to the quasi-streamwise vortices. Roughness affects the anisotropy of the vorticity tensor near the wall. The peaks of $\omega'_{y,rms}$ and $\omega'_{z,rms}$ are significantly lower

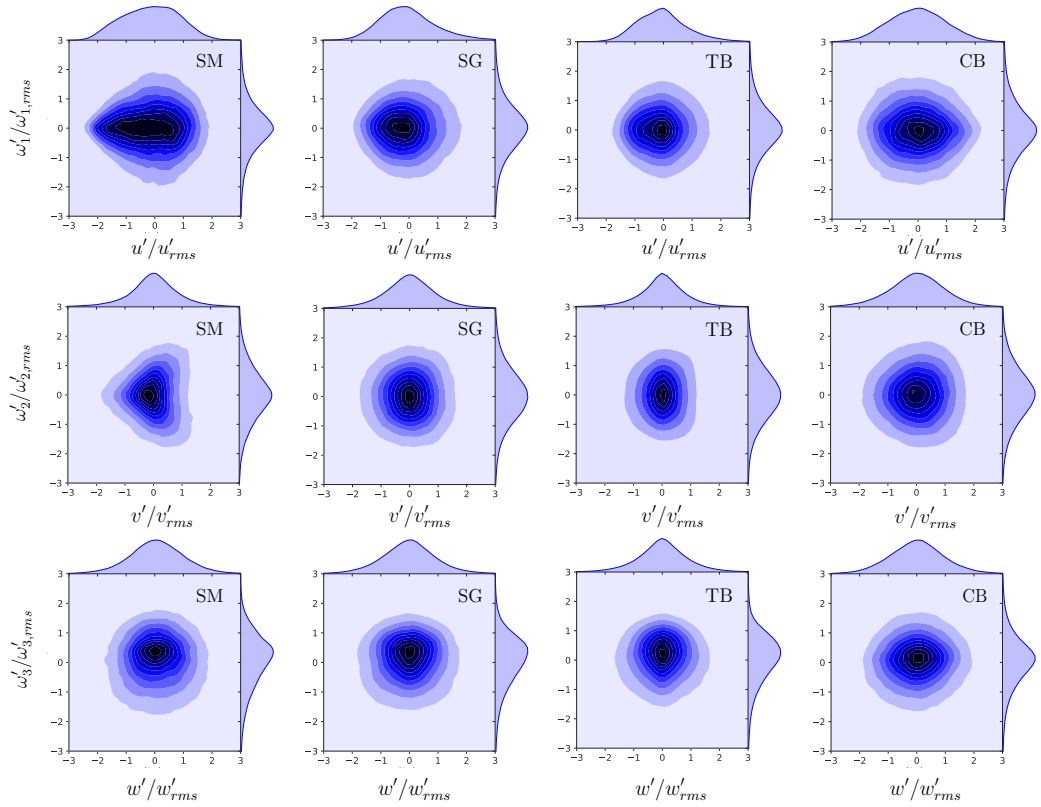

Figure 14. Joint PDFs of instantaneous values of u'_α and ω'_α, normalized by their respective RMS values; data are from the wall-parallel plane at $y^+ = 15$ for smooth-wall flow and $y = d$ for SG, TB and CB roughness.

in flow over rough walls compared to smooth ones, implying that roughness modifies the organized motions by breaking down the near-wall streaks and promoting the three-dimensionality of the vortical motions. SG and CB roughnesses have a similar effect on producing significantly more isotropic vorticity fluctuations. In contrast, ω_i' near the TB roughness maintains a high anisotropy similar to the smooth wall. This is because that, for TB roughness, low-speed streaks with intense u' are still present below $y = d$ in the recessed roughness region (due to the largest x and z wavelengths of the surface). The behavior of TB roughness is again shown to be intermediate to that of smooth wall and SG roughness.

The joint probability density functions (PDFs) of u'_α and ω'_α, which contribute to the local helicity $u'_\alpha\omega'_\alpha$, are compared in Figure 14. Data are plotted at $y = d$ for SG, TB and CB roughness and at $y^+ = 15$ for the smooth surface. Three types of turbulent eddies have been defined by Kassinos [55] as: jetal ($u'_\alpha \neq 0$, $\omega'_\alpha \approx 0$); vortical ($u'_\alpha \approx 0$, $\omega'_\alpha \neq 0$); and helical ($u'_\alpha \neq 0$, $\omega'_\alpha \neq 0$). The joint PDF for the flow over the smooth wall is skewed towards jetal motions with $u' < 0$ and $\omega'_1 \approx 0$, which is the characteristic of the low-speed streaks. Roughness, irrespective of its texture, reduces the significance of these motions and makes the joint PDF contours more concentric. In the case of CB roughness, a slight tendency exists towards positive values of u', which may suggest slightly more pronounced sweeping events at $y \approx d$. The joint PDFs of v' and ω'_2 shows that, at $y^+ = 15$ on the smooth wall, the v' motions are dominantly associated with jetal sweeps ($v' < 0$, $\omega'_2 \approx 0$), inactive motions originated from above, and helical ejection motions ($v' > 0$, $\omega'_2 \neq 0$), representing the counter-rotating pairs of quasi-streamwise vortices. Near roughness, in contrast, all types of motions are roughly equally possible, indicating highly three-dimensional shape of coherent motions. The joint PDFs of w' and ω'_3 show a symmetric behavior for all cases, on account of the symmetry due to the boundary conditions in this direction. Joint PDFs were also obtained in the outer layer at $y/\delta = 0.3$ and were all very similar (not shown), consistent with Townsend's similarity hypothesis.

3.5. Instantaneous vortical motions and conditional eddies

Instantaneous coherent motions were visualized using iso-surfaces of their swirl strength, quantified by the imaginary part of the complex eigenvalue of the velocity gradient tensor λ_{ci} [6]. The results are shown in Figure 15 for $y/\delta < 0.25$, in which it can be seen that inclined quasi-streamwise vortices exist in the vicinity of both smooth and rough walls, with higher inclination angles (in the $x - y$ plane) and tilt angles (in the $x - z$ plane), as well as more irregular shape for SG and CB roughnesses. Large number of spanwise-aligned vortex segments are also visible on the rough surfaces. On SG and CB surfaces, two arch-shape vortical structures are highlighted, which are thought to be examples of the solid-body rotation of an originally head-down horse-shoe vortex on account of strong local shear layer, to be discussed in Section 3.6.

Linear stochastic estimation (LSE) [4] was used to compare the vortex shape over both the smooth wall [6, 56] and rough ones [2, 57]. Instead of obtaining the domain-averaged field conditioned on a given event at specified locations as used by Adrian [58], we calculate such averaged field conditioned on a given event at all (x, z) locations at a reference elevation. The advantage of such approach is that the conditional eddy obtained herein is composed of all possible physical eddies associated with the events; an overall picture can be formed on how all types of relevant eddies are modified

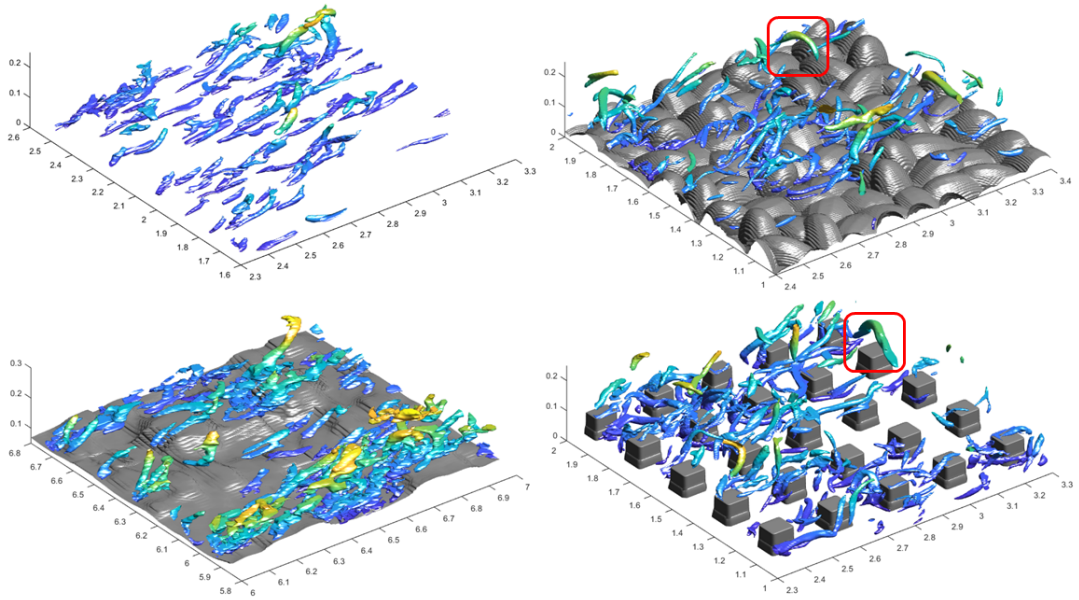

Figure 15. Instantaneous vortical motions, visualized by iso-surfaces of $\lambda_{ci} = 0.2\lambda_{ci,max}$, colored according to distance from the wall.

by the roughness, which is especially helpful for a qualitative comparison of vortex shape around random roughness geometries. It is also noted that the limitation of such approach is that it does not offer location-specific information on the shape of relevant eddies. Here, we use an event based on the vortex-identification parameter, following Talapatra and Katz [2]. The conditional velocity field at displacement $\boldsymbol{r}$ from the point $\boldsymbol{x}$ is determined as

$$\left\langle \boldsymbol{u'}(\boldsymbol{x}+\boldsymbol{r}) \middle| \lambda'_{ci}(\boldsymbol{x}) > 0 \right\rangle \Big|_{\lambda'_{ci}=\lambda'_{ci,s}} = \frac{\left\langle \boldsymbol{u'}(\boldsymbol{x}+\boldsymbol{r})\lambda'_{ci}(\boldsymbol{x}) \right\rangle}{\left\langle \lambda'_{ci}(\boldsymbol{x})\lambda'_{ci}(\boldsymbol{x}) \right\rangle} \lambda'_{ci,s}, \tag{9}$$

with $\lambda_{ci} > 0$ being the event. Here, $\lambda'_{ci,s}$ is equal to one and acts as a dummy variable, since the results shown in the visualizations are normalized. From this conditionally-averaged flow field, the shape of the coherent motions is obtained as the isosurface of the swirling strength and shown in Figures 16 at various elevations for all cases. A sensitivity analysis was carried out to ensure that the overall comparison of vortex shape is independent of the thresholds used. The near-wall elevations compare $y^+ = 15$ and 40 in the smooth case with $y = d$ and $y = k_c$ in the rough cases. The outer-layer elevation is located at $y/\delta = 0.2$. Note that, in Figures 16, the rough surfaces are for illustration of the size and elevation of the eddies only, not to show the exact (x, z) locations of such coherent motions.

In the buffer layer ($y^+ = 15$) of the smooth case, the conditional eddy comprises pairs of inclined streamwise-aligned vortices, with a bifurcation. This is because the quasi-streamwise vortices are not strictly aligned in x but tilted toward both positive and negative z-directions with equal probabilities [5]. The conditional eddy at $y = d$ for TB roughness is similar to the smooth case because the quasi-streamwise vortices are also present in the troughs of δ-scale undulations of this roughness. Such near-wall similarity suggests that turbulence in flow over TB roughness obeys a similar

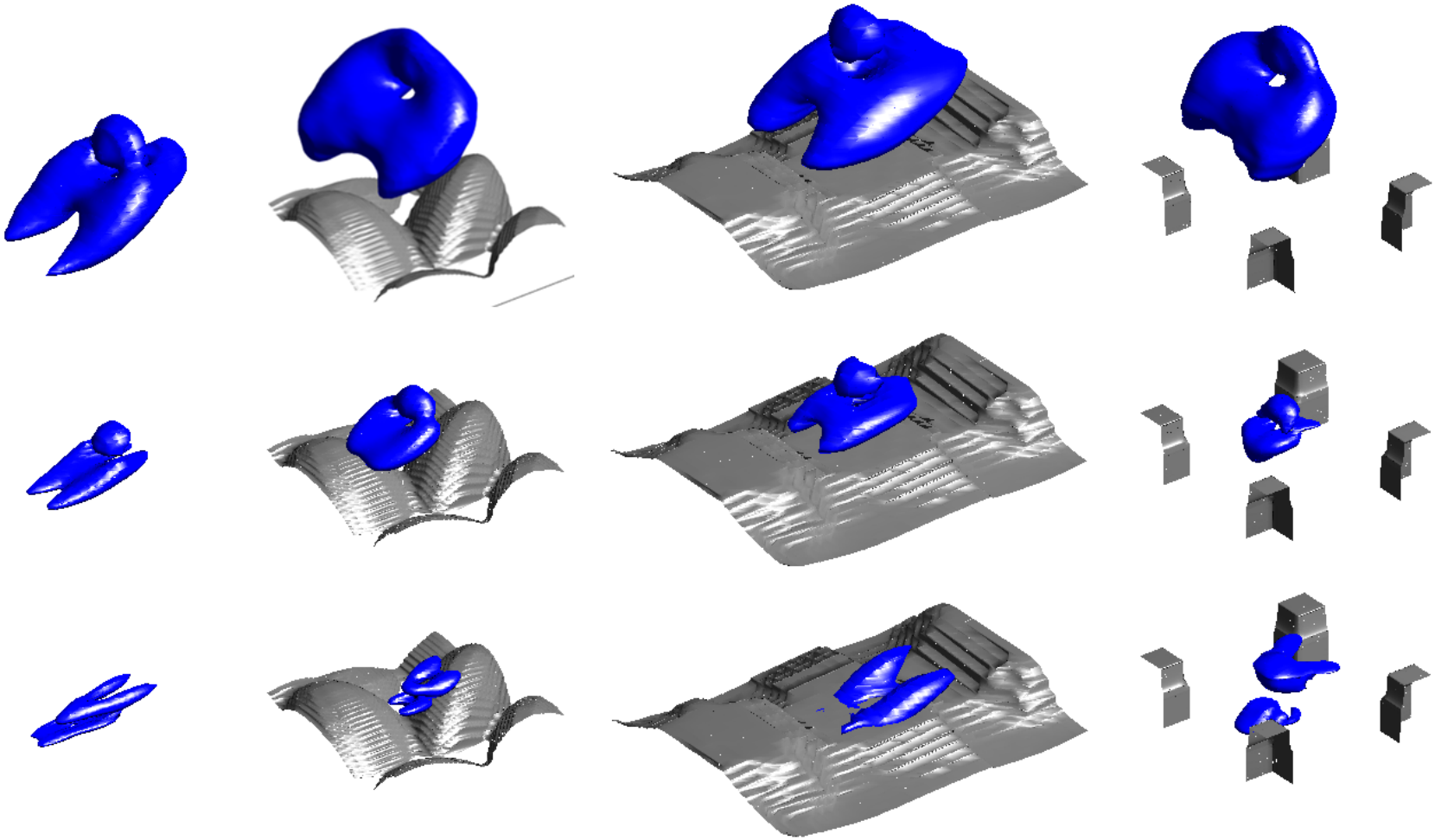

Figure 16. Conditional eddies based on an event of $\lambda_c > 0$, at three y locations; from bottom to top, $y^+ = 15$, $y^+ = 40$, $y/\delta = 0.1$ for SM; and $y = d$, $y = k_c$, $y = 0.2\delta$ for SG, TB and CB roughness. Plots are iso-surfaces of $\lambda_{ci} = 0.4$ obtained from the conditional velocity field.

growth mechanism to that in smooth-wall flows, such as the streak transient growth mechanism of Schoppa and Hussain [59].

At $y = d$, both the SG and CB cases show a pair of vortices with three-dimensional shapes. For SG roughness, it is evident that a head-up and a head-down U-shape vortices are both present. The lower vortex appears to represent the vortex formed due to shear-layer roll-up wrapping around the recirculation region downstream of a roughness element [60]. The upper vortex appears similar to the head-down horse-shoe vortex observed by Talapatra and Katz [2], which is formed as both ends of an incoming spanwise-aligned vortex undergo stretching in x (due to mean-flow channeling on both sides of the cube) and lifting (due to interactions with the adjacent vortices of the same kind). This similarity in conditional-eddy shape between SG and CB roughness is thought to be a consequence of both surfaces featuring distinct roughness elements with high values of local surface slope. Thus both kinds of roughness cause significant channeling phenomena and recirculation behind roughness elements.

In the overlap regions and above ($y \geq 40$ for the smooth case and $y \geq y_R$ for the rough cases), the conditional eddies of all cases display connection between the pair of parallel vortices, comprising spanwise-aligned portions that resemble the horse-shoe heads. In the outer layer ($y/\delta > 0.1$), the size of such outer-layer conditional eddy is similar regardless of the surface. At such elevation, the main difference in the vortex shape is that the legs are shorter on the rough walls than those on the smooth wall, due to the higher three-dimensionality and inclination angles of individual vortices on rough walls as shown in Figure 15.

A comparison of the size of the conditional eddies shows that, far from the wall, spanwise spatial extents of the eddies are all very similar, while the streamwise extents are slightly shorter for SG and CB roughnesses compared to TB roughness and the smooth wall due to the shortened legs. Near the wall, shorter x extents of the vortical motions are also observed on SG and CB compared to TB and the smooth wall, possibly resulting from the difference in eddy shape and orientation. The z extents, however, are larger in the cases of TB and CB roughnesses, as these two roughness geometries impart larger spanwise length scales into the flow.

3.6. A kinematic process of vortices in local shear layers

We describe a process undergone by vortical motions around CB roughness (and probably, to a lesser extent, around SG roughness also) that is thought to contribute to local TKE production and to a shorter x-extent of coherence compared to the smooth and TB cases. Without loss of generality, the CB roughness is used for illustration. A sketch is shown in Figure 17 (a). As the head-down horse-shoe vortex wrapping around a cube element (vortex B) develops from an incoming spanwise vortex (vortex A)—similar to the process described by Talapatra and Katz [2]—the head of this vortex is lifted (by convection) by the mean-flow ejection immediately upstream of the cube (where $\overline{v} > 0$), while the legs are convected both downstream (due to channeling phenomenon, $\widetilde{u} > 0$ on both sides of the cube) and upward (due to mutual induction between adjacent legs). The resultant vortex may take a shape similar to that of Vortex C. As the head portion of vortex C moves downstream near the top surface of the cube, it is subject to intense time-mean spanwise vorticity Ω_z of a negative sign. Consequently, the head potion undergoes clockwise solid-body rotation. Meanwhile, the leg portions of vortex C, as they are inclined upward, undergo stretching by positive $\partial\langle\overline{u}\rangle/\partial y$ and quickly break down due to non-linear interaction with other vortices.

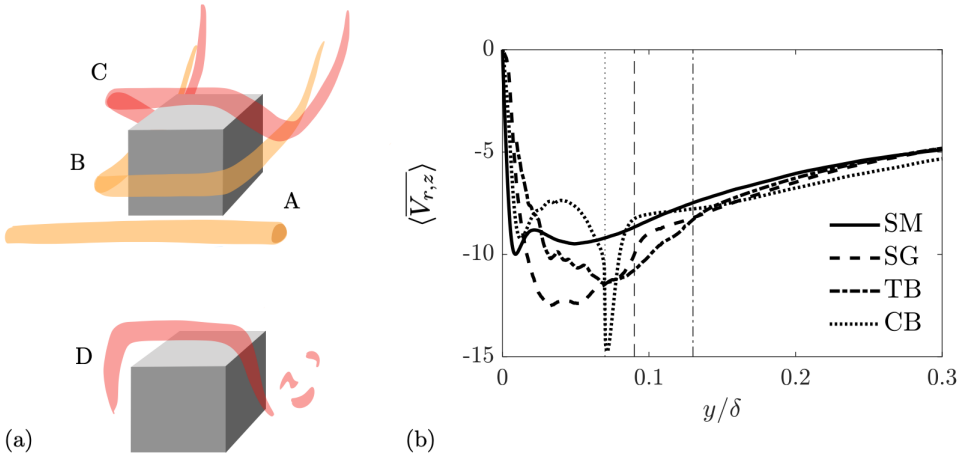

Figure 17. (a) Sketch of evolution of a spanwise vortex approaching a cube element. (b) Wall-normal profiles of $\langle\overline{V_{r,z}}\rangle$ normalized by u_τ and δ; vertical lines indicate crest height for each rough case.

The result is a significantly shorter extent in x of the coherent motions (vortex D). In the averaged eddy conditioned at elevation of k_c shown in Figure 16, the aforementioned vortical motion may manifest itself as the arch-shaped structure roughly oriented in the (x, z) plane. Examples of instantaneous vortices possibly of this type are highlighted in Figure 15. Such process is a result of relatively flat top surface of a horizontally sizable roughness element; the local elevation of this surface into the flow (and the strong local Ω_z in its vicinity as a result) leads to the aforementioned solid-body rotation of the vortex. For the TB roughness with mostly sharp protuberances, this process is probably less pronounced.

In the following, evidences are provided to support the existence of such z-aligned vortices located in the vicinity of the top surface of a cube. First, the eddy axis of vortices around the cube is quantified, in an average sense, by an identifier inferred from the eddy-visualization method of Zhou *et al.* [6],

$$\boldsymbol{V}_r(\boldsymbol{x}, t) = -\boldsymbol{v}_r(\boldsymbol{x}, t)\lambda_{ci}(\boldsymbol{x}, t), \tag{10}$$

where $\boldsymbol{v}_r$, a unit vector, is the normal eigenvector of the velocity-gradient tensor corresponding to the real eigenvalue (the other two eigenvalues being complex conjugates by definition of swirling motion). $\boldsymbol{V}_r$ weighs the local rotation-axis direction of an eddy with its local rotational strength λ_{ci} about this axis. Thus, a high magnitude of the time-averaged value of its i component, $|\overline{V_{r,i}}|(\boldsymbol{x})$, indicates local strong swirling motion around the x_i axis in an average sense. The wall-normal profiles of the z component of the spatially-averaged $\overline{\boldsymbol{V}}_r$ are compared in Figure 17 (b) among all cases. The high-magnitude peak of $\langle\overline{V_{r,z}}\rangle$ (with a negative sign) located at the crest level of CB roughness indicates significant strength of z-aligned, clockwise-rotating vortices at this elevation. In contrast, no peak of $|\overline{V_{r,z}}|$ is observed at the crest level for the other two roughness geometries. In addition, the spatial distribution of $\overline{V_{r,z}}$ around CB roughness in Figure 18 (a) shows that z-aligned eddies with high swirling strengths are found in the regions immediately upstream of a cube element and near its top surface; such eddies are also prevalent in the wake region of a cube. Moreover, in Figure 18 (b), it is shown that regions of strong Ω_z of the negative sign coincide with the region with strong $|\overline{V_{r,z}}|$ (Figure 18(a)) near the top surface of a cube. These evidences sup-

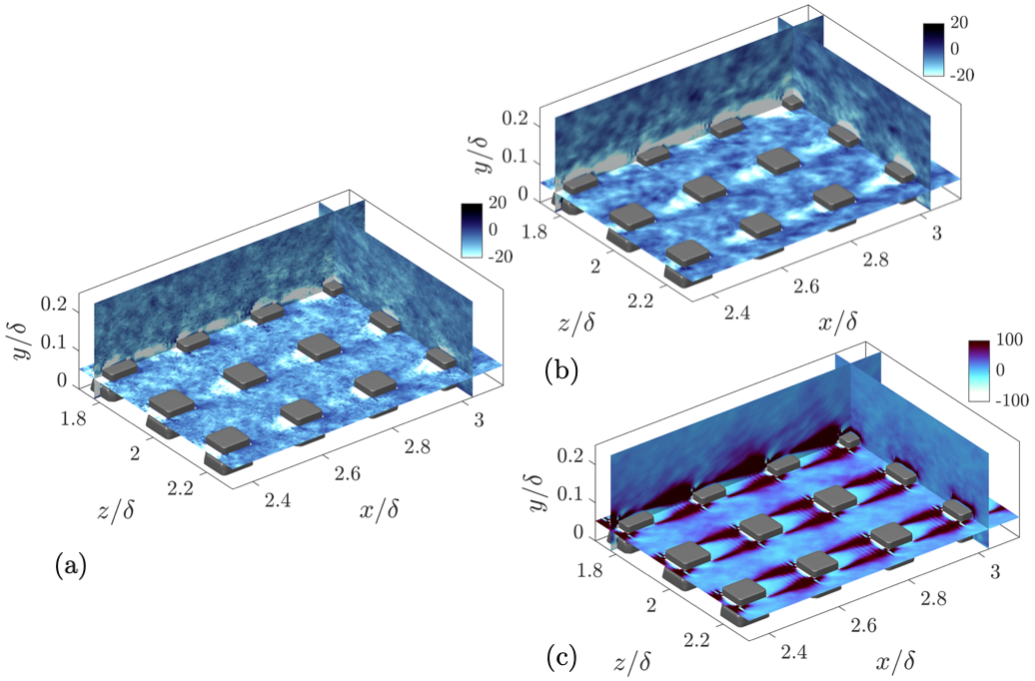

Figure 18. Contours of Ω_z (a), $\overline{V}_{r,z}$ (b) and time-averaged shear production of TKE (c) for CB roughness. Normalization is done using u_τ and δ.

port the existence of the aforementioned solid-body rotation process of the head-down horse-shoe vortex head, which leads to a shortened x-extent of coherent motions.

Another significance of this process is that it is expected to yield significant TKE production at the top surface of a cube. At this location the spanwise-aligned head of vortex C and vortex D in Figure 17 (a) together with the two legs induces intense Q4 motions, which yields significant local shear production of TKE in the background of the strong $\partial\overline{u}/\partial y$ values within the thin shear layer. The spatial distribution of local shear production of TKE, $P_{s,ii}/2 = \overline{u_i'u_j'}\partial\overline{u_i}/\partial x_j$ is plotted in Figure 18 (c), indeed showing high values in the vicinity of the top surface of a cube element.

4. Concluding remarks

Turbulence structures in fully-developed channel flows at $Re_\tau = 1000$ have been analyzed for flow over a smooth wall (SM), and flows over a realistic turbine-blade surface (TB), a sandgrain surface (SG), and a k-type cube (CB) surface. The results presented in the paper appear to be consistent with the following qualitative description of turbulent boundary layers over rough surfaces. When compared to flow over a smooth surface, the bulk drag force over each rough surface considered here (Table 1) is significantly larger. It is because the increase in form drag caused by the particular size, shape, and distribution of roughness elements exceeds the corresponding reduction in viscous drag on account of roughness-induced disruption of the viscous sublayer [42]. The magnitude of the increase in form drag depends upon the individual surface roughness topography and, in this study, is approximately twice as large for SG and CB roughness as it is for TB roughness. The second principal effect of surface rough-

ness is to modify near wall coherent motions and, consequently, to modify turbulent processes in this region. The penetration extent of roughness effects is mostly in the roughness sublayer, however it can go beyond this region depending on the type of the roughness, due to the limited δ/k_c ratio. The significant modifications on near wall coherent motions, caused by different roughness geometries presented here, are: *i*) the smooth-wall quasi-streamwise vortices are retained over TB roughness within δ-scale undulations, whereas they are replaced by a pair of 'head-up, head down' horse-shoe vortices over SG and CB rough surfaces. *ii*) The longitudinal extent of near wall structures over smooth wall is retained in the TB roughness, but it is shortened significantly for SG and CB rough surfaces, which is in part, if not predominantly, due to a solid-body rotation process of the head-down horse-shoe vortices on account of the strong shear layer above a roughness protuberance. This effect is inherited to the vortical motions in the roughness sublayer and beyond that. Evidence supporting the existence of such process in case CB is provided by analyses of linear stochastic estimation and eddy-axis-of-rotation. The results suggest that the process concerns a considerable amount of eddies at crest location, and may have a substantial influence on turbulence intensities and shear production of turbulent kinetic energy. *iii*) The effect of shortened structures in flows over SG and CB is to reduce the energy level at low wavenumbers (energy containing eddies), while increasing energy level at higher wavenumbers, which are closer to the dissipative scales. In stationary turbulent flows, the enhanced dissipation requires enhanced production of turbulent energy (required by equilibrium condition), leading to increase in drag work, on account of surface roughness.

The strong dependence of the near-wall flow on surface texture is also revealed by profiles of $R_{u_i u_j,n}$, which exhibit surface periodicity, and velocity spectra which contrast the different cascades of energy from large-scale to small-scale motions for rough and smooth wall flows. Joint PDF profiles of $(u'_\alpha, \omega'_\alpha)$ show that roughness weakens low-speed streaks and results in roughly equal possibilities for all types of motions, yielding more isotropic flow in this region. Roughness also increases the inclination angles of large-scale structures near the surface. At $y = d$, conditional eddies obtained by linear stochastic estimation are very similar for flow over smooth walls and TB roughness: two bifurcated streamwise vortices. For flow over SG and CB roughness, they are a pair of horse-shoe structures, one on top of the other. The lower one is conjectured to be produced by shear-layer roll-up in the wake behind roughness elements, and the upper one is similar to the U-shape structure observed by Talapatra and Katz [2], which is produced by vortex stretching due to flow channeling.

In the outer boundary layer, Townsend's similarity appears to apply to the single-point statistics, the average inclination angles of energy-containing coherent motions, velocity spectra, helicity characteristics (joint PDF of u'_α, ω'_α) and the average shape of turbulent eddies. However streamwise two-point velocity correlations and associated length scales are surface-texture dependent in this region, probably due to the limited δ/k_c herein. Streamwise length scales, obtained by profiles of $R_{u_i u_j,n}$ and conditional eddies, for SG and CB roughness are shorter than those over smooth walls and TB roughness.

The results discussed in this paper are for the values of turbulent Reynolds number and δ/k_c permitted by today's capabilities in direct numerical simulations. A more detailed understanding of the near wall physics and its connection to the outer-layer region for flows over rough walls at higher values of Re_τ and δ/k_c, having satisfied the expectations of both direct numerical simulations and fully-rough condition, remains an interesting challenge for the future. The future work also includes structural

comparison with various roughness textures with matching k_s^+ (or the drag).

Acknowledgements

The authors gratefully acknowledge the financial support of the Office of Naval Research (Award No. N00014-17-1-2102) and the computational resources provided by Institute for Cyber-Enabled Research, Michigan State University.

References

[1] Townsend AA. The structure of turbulent shear flow. Cambridge University Press; 1976.

[2] Talapatra S, Katz J. Coherent structures in the inner part of a rough-wall channel flow resolved using holographic PIV. J Fluid Mech. 2012;711:161–170.

[3] Robinson SK. Coherent motions in the turbulent boundary layer. Annu Rev Fluid Mech. 1991;23(1):601–639.

[4] Adrian RJ. On the role of conditional averages in turbulence theory. Turbulence in Liquids, Science press. 1975;:323–332.

[5] Jeong J, Hussain F, Schoppa W, et al. Coherent structures near the wall in a turbulent channel flow. J Fluid Mech. 1997;332:185–214.

[6] Zhou J, Adrian RJ, Balachandar S, et al. Mechanisms for generating coherent packets of hairpin vortices in channel flow. J Fluid Mech. 1999;387:353–396.

[7] Lozano-Durán A, Jiménez J. Time-resolved evolution of coherent structures in turbulent channels: characterization of eddies and cascades. J Fluid Mech. 2014; 759:432471.

[8] Wu X, Moin P, Wallace JM, et al. Transitional–turbulent spots and turbulent–turbulent spots in boundary layers. Proceedings of the National Academy of Sciences. 2017;:E5292–E5299.

[9] Tardu S. Transport and coherent structures in wall turbulence. Wiley & Sons, Inc.; 2014.

[10] Coceal O, Dobre A, Thomas TG, et al. Structure of turbulent flow over regular arrays of cubical roughness. J Fluid Mech. 2007;589:375–409.

[11] Wu Y, Christensen KT. Spatial structure of a turbulent boundary layer with irregular surface roughness. J Fluid Mech. 2010;655:380–418.

[12] Volino RJ, Schultz MP, Flack KA. Turbulence structure in boundary layers over periodic two- and three-dimensional roughness. J Fluid Mech. 2011;676:172–190.

[13] Chan L, MacDonald M, Chung D, et al. Secondary motion in turbulent pipe flow with three-dimensional roughness. J Fluid Mech. 2018;854:533.

[14] Krogstad PÅ, Antonia RA. Surface roughness effects in turbulent boundary layers. Exp Fluids. 1999;27(5):450–460.

[15] Passalacqua P, Porté-Agel F, Foufoula-Georgiou E, et al. Application of dynamic subgrid-scale concepts from large-eddy simulation to modeling landscape evolution. Water Resour Res. 2006;42:W06D11–1–11.

[16] Orlandi P, Leonardi S, Antonia RA. Turbulent channel flow with either transverse or longitudinal roughness elements on one wall. J Fluid Mech. 2006;561:279–305.

[17] Forooghi P, Stroh A, Schlatter P, et al. Direct numerical simulation of flow over dissimilar, randomly distributed roughness elements: A systematic study on the

effect of surface morphology on turbulence. Phys Rev Fluids. 2018 Apr;3:044605. Available from: https://link.aps.org/doi/10.1103/PhysRevFluids.3.044605.
[18] Barros JM, Schultz MP, Flack KA. Measurements of skin-friction of systematically generated surface roughness. International Journal of Heat and Fluid Flow. 2018;72:1 – 7. Available from: http://www.sciencedirect.com/science/article/pii/S0142727X17312584.
[19] Yuan J, Piomelli U. Estimation and prediction of the roughness function on realistic surfaces. J Turbul. 2014 October;15:350–365. Available from: http://hdl.handle.net/1974/6846.
[20] Busse A, Lützner M, Sandham ND. Direct numerical simulation of turbulent flow over a rough surface based on a surface scan. Comput Fluids. 2015;116:129–147.
[21] Scotti A. Direct numerical simulation of turbulent channel flows with boundary roughened with virtual sandpaper. Phys Fluids. 2006;18:031701–1—4.
[22] Yuan J, Piomelli U. Numerical simulations of sink-flow boundary layers over rough surfaces. Phys Fluids. 2014;26:015113–1—015113–28.
[23] Yuan J, Piomelli U. Roughness effects on the reynolds stress budgets in near-wall turbulence. J Fluid Mech. 2014;760:R1.
[24] Keating A. Large-eddy simulation of heat transfer in turbulent channel flow and in the turbulent flow downstream of a backward-facing step [dissertation]. University of Queensland; 2004.
[25] Raupach MR, Shaw RH. Averaging procedures for flow within vegetation canopies. Bound-Lay Meteorol. 1982;22:79–90.
[26] Leonardi S, Orlandi P, Antonia RA. Properties of d- and k-type roughness in a turbulent channel flow. Physics of Fluids. 2007;19(12):125101. Available from: https://doi.org/10.1063/1.2821908.
[27] Napoli E, Armenio V, De Marchis M. The effect of the slope of irregularly distributed roughness elements on turbulent wall-bounded flows. J Fluid Mech. 2008; 613:385–394.
[28] Yuan J, Aghaei Jouybari M. Topographical effects of roughness on turbulence statistics in roughness sublayer. Phys Rev Fluids. 2018 Nov;3:114603–19. Available from: https://link.aps.org/doi/10.1103/PhysRevFluids.3.114603.
[29] Majumdar A, Bhushan B. Role of fractal geometry in roughness characterization and contact mechanics of surfaces. ASME J Tribol. 1990;112(2):205–216.
[30] Bandyopadhyay PR. Rough-wall turbulent boundary layers in the transition regime. J Fluid Mech. 1987;180:231–266.
[31] Moser RD, Moin P. The effects of curvature in wall-bounded turbulent flows. J Fluid Mech. 1987;175:479–510.
[32] Pokrajac D, Campbell LJ, Nikora V, et al. Quadrant analysis of persistent spatial velocity perturbations over square-bar roughness. Exp Fluids. 2007;42:413–423.
[33] Schultz MP, Flack KA. Reynolds-number scaling of turbulent channel flow. Phys Fluids. 2013;25:025104–1—13.
[34] Nikuradse J. Laws of flow in rough pipes. NACA Technical Memorandum 1292. 1933;.
[35] Jackson PS. On the displacement height in the logarithmic velocity profile. J Fluid Mech. 1981;111:15–25.
[36] Mejia-Alvarez R, Christensen KT. Low-order representations of irregular surface roughness and their impact on a turbulent boundary layer. Phys Fluids. 2010; 22:015106–1—20.
[37] Barros JM, Christensen KT. Observations of turbulent secondary flows in a rough-wall boundary layer. J Fluid Mech. 2014;748:R1.

[38] Vanderwel C, Ganapathisubramani B. Effects of spanwise spacing on large-scale secondary flows in rough-wall turbulent boundary layers. J Fluid Mech. 2015; Accepted.
[39] Yang J, Anderson W. Numerical study of turbulent channel flow over surfaces with variable spanwise heterogeneities: Topographically-driven secondary flows affect outer-layer similarity of turbulent length scales. Flow, Turb Combust. 2018; 100:1–17.
[40] Munters W, Meneveau C, Meyers J. Shifted periodic boundary conditions for simulations of wall-bounded turbulent flows. Phys Fluids. 2016;28:025112.
[41] Leonardi S, Orlandi P, Djenidi L, et al. Structure of turbulent channel flow with square bars on one wall. Int J Heat Fluid Flow. 2004;25:384–32.
[42] Jiménez J. Turbulent flows over rough walls. Annu Rev Fluid Mech. 2004;36:173–196.
[43] Krogstad PÅ, Antonia RA. Structure of turbulent boundary layers on smooth and rough walls. J Fluid Mech. 1994;277:1–21.
[44] Christensen KT, Wu Y. Characteristics of vortex organization in the outer layer of wall turbulence. In: Proc. Fourth Int. Symp. on Turbulence and Shear Flow Phenomena; Vol. 3; Williamsburg, Virginia; 2005. p. 1025–1030.
[45] Sabot J, Saleh I, ComteBellot G. Effects of roughness on the intermittent maintenance of reynolds shear stress in pipe flow. The Physics of Fluids. 1977;20(10):S150–S155. Available from: https://aip.scitation.org/doi/abs/10.1063/1.861724.
[46] Tomkins CD, Adrian RJ. Spanwise structure and scale growth in turbulent boundary layers. J Fluid Mech. 2003;490:37–74.
[47] del Álamo JC, Jiménez J, Zandonade P, et al. Scaling of the energy spectra of turbulent channels. J Fluid Mech. 2004;500:135 – 144.
[48] Hoyas S, Jiménez J. Reynolds number effects on the Reynolds-stress budgets in turbulent channels. Phys Fluids. 2008;20:101511–1–9.
[49] Krogstad PÅ, Efros V. About turbulence statistics in the outer part of a boundary layer developing over two- dimensional surface roughness. Phys Fluids. 2012; 24:075112–1—15.
[50] Kolmogorov AN. The local structure of turbulence in incompressible viscous fluid for very large reynolds number. Dokl Akad Nauk SSSR. 1941;30:299–303.
[51] Ganapathisubramani B, Hutchins N, Hambleton WT, et al. Investigation of large-scale coherence in a turbulent boundary layer using two-point correlations. J Fluid Mech. 2005;524:57–80.
[52] Jiménez J, Hoyas S, Simens MP, et al. Turbulent boundary layers and channels at moderate reynolds numbers. J Fluid Mech. 2010;657:335–360.
[53] Moser RD, Kim J, Mansour NN. Direct numerical simulation of turbulent channel flow up to $Re_\tau = 590$. Phys Fluids. 1999;11(4):943–945. Available from: http://link.aip.org/link/?PHF/11/943/1.
[54] Bhaganagar K, Kim J, Coleman G. Effect of roughness on wall-bounded turbulence. Flow, Turbulence and Combustion. 2004 Jul;72(2):463–492.
[55] Kassinos SC. A structure-based model for the rapid distortion of homogeneous turbulence [dissertation]. Stanford University; 1995.
[56] Adrian RJ. Hairpin vortex organization in wall turbulence. Phys Fluids. 2007; 19:041301.
[57] Hong J, Katz J, Schultz MP. Near-wall turbulence statistics and flow structures over three-dimensional roughness in a turbulent channel flow. J Fluid Mech. 2011; 667:1–37.

[58] Adrian RJ. Stochastic estimation of the structure of turbulent fields. Vienna: Springer Vienna; 1996. p. 145–195.
[59] Schoppa W, Hussain F. Coherent structure generation in near-wall turbulence. J Fluid Mech. 2002;453:57–108.
[60] Manhart M. Vortex shedding from a hemisphere in a turbulent boundary layer. Theoretical and Computational Fluid Dynamics. 1998 Jul;12(1):1–28. Available from: https://doi.org/10.1007/s001620050096.